Wave chaos in a randomly inhomogeneous waveguide: Spectral analysis of the finite-range evolution operator

D. V. Makarov,[1,*] L. E. Kon'kov,[1] M. Yu. Uleysky,[1] and P. S. Petrov[1,2]

[1]*V.I. Il'ichev Pacific Oceanological Institute of the Far-Eastern Branch of the Russian Academy of Sciences, 43 Baltiyskaya St., 690041 Vladivostok, Russia*

[2]*Far Eastern Federal University, 8 Sukhanova St., 690950 Vladivostok, Russia*

(Received 23 March 2012; revised manuscript received 10 December 2012; published 22 January 2013)

The problem of sound propagation in a randomly inhomogeneous oceanic waveguide is considered. An underwater sound channel in the Sea of Japan is taken as an example. Our attention is concentrated on the domains of finite-range ray stability in phase space and their influence on wave dynamics. These domains can be found by means of the one-step Poincare map. To study manifestations of finite-range ray stability, we introduce the finite-range evolution operator (FREO) describing transformation of a wave field in the course of propagation along a finite segment of a waveguide. Carrying out statistical analysis of the FREO spectrum, we estimate the contribution of regular domains and explore their evanescence with increasing length of the segment. We utilize several methods of spectral analysis: analysis of eigenfunctions by expanding them over modes of the unperturbed waveguide, approximation of level-spacing statistics by means of the Berry-Robnik distribution, and the procedure used by A. Relano and coworkers [Relano *et al.*, Phys. Rev. Lett. **89**, 244102 (2002); Relano, *ibid.* **100**, 224101 (2008)]. Comparing the results obtained with different methods, we find that the method based on the statistical analysis of FREO eigenfunctions is the most favorable for estimating the contribution of regular domains. It allows one to find directly the waveguide modes whose refraction is regular despite the random inhomogeneity. For example, it is found that near-axial sound propagation in the Sea of Japan preserves stability even over distances of hundreds of kilometers due to the presence of a shearless torus in the classical phase space. Increasing the acoustic wavelength degrades scattering, resulting in recovery of eigenfunction localization near periodic orbits of the one-step Poincaré map.

DOI: 10.1103/PhysRevE.87.012911 PACS number(s): 05.45.Mt, 43.30.Cq, 03.65.Yz, 05.45.Ac

I. INTRODUCTION

It was recognized many years ago that low-dimensional deterministic dynamical systems can exhibit chaotic behavior, and chaos reveals itself in physical properties. A typical dynamical system is characterized by a mixed phase space with the coexistence of regular and chaotic domains. If the Hamiltonian of the system contains a randomlike time-dependent perturbation with broad spectrum, regular domains cannot survive for an infinite time interval, except for some atypical situations. However, there can be domains of finite-time stability whose lifetimes can be sufficiently large. Such domains play an essential role in transport properties. Their influence results in emergence of nonequilibrium quasistationary states in many-body systems like the HMF model [1,2], transport barriers for charged particles in weakly turbulent electric and magnetic fields [3], or Lagrangian coherent structures like coherent clusters for passive scalars or eddies in randomly inhomogeneous hydrodynamic flows [4], to name a few well-known examples. Domains of finite-time stability can be directly found using phase-space distributions of finite-time Lyapunov exponents [5,6]. Alternatively, one can invoke the procedure proposed in Ref. [7] or calculate eigenfunctions of the Perron-Frobenius operator [8,9]. Although these methods provide good quantitative accuracy, they are purely numerical and do not describe the origin of regular domains. A different approach had been proposed in Ref. [10,11], where dynamics of a randomly perturbed classical dynamical system under a single realization of the random perturbation was studied using the so-called one-step (or specific) Poincaré map. This map allows one to estimate analytically the lifetime of stable domains using the theory of time-periodic Hamiltonian systems. In Refs. [12,13], the one-step Poincaré map had been generalized onto classical dynamical systems with dissipation.

Using the basic principles of the quantum-classical correspondence, the concept of the one-step Poincaré map can be generalized onto quantum systems. In this case, the role of the one-step Poincaré map is played by the finite-time evolution operator. In quantum systems, presence of long-living regular domains in the classical phase space implies the existence of wave packets which do not exhibit chaos-assisted spreading for relatively long times. Finite-time stability manifests itself in spectral properties of the finite-time evolution operator, in particular, in level-spacing statistics [14]. A spatial analog of the finite-time evolution operator, related to the problem of wave propagation in randomly inhomogeneous waveguides, had been introduced in Ref. [15]. This operator was referred to as the finite-range evolution operator (FREO). According to Ref. [15], the applicability of level-spacing statistics for studying of transition to chaos depends on spatial structure of the perturbation induced by random inhomogeneity. For example, when the perturbation is smooth along the transversal coordinate, the transformation of level-spacing statistics can properly describe transition to chaos with increasing propagation range [15]. In the opposite case of fast transversal perturbation oscillations, analysis of level spacings can be misleading due to proliferation of nearly degenerate levels, whose occurrence is caused by the cascade of classical bifurcations.

*makarov@poi.dvo.ru

The present paper is devoted to further development of the approach used in Refs. [14,15]. We concentrate our attention on analysis of FREO eigenfunctions and propose the method which allows one to find directly waveguide modes corresponding to regular propagation. Quantitative estimates of wave chaos, obtained via the eigenfunction analysis, are not affected by limitations imposed by classical bifurcations. In addition, we use in the present work two methods of eigenvalue analysis and compare the results obtained with different methods.

As in Ref. [15], we consider the problem of sound propagation in the ocean as an example. It is realized that small sound-speed variations induced by oceanic internal waves lead to Lyapunov instability and chaos of sound rays. In the mathematical sense, ray chaos is an analog of classical chaos in Hamiltonian systems. Indeed, ray motion in a waveguide is equivalent to motion of a point particle in a potential well, and sound-speed variations along a waveguide play the role of a nonstationary perturbation. Reciprocal Lyapunov exponent for chaotic rays typically is of about several tens or hundreds kilometers [16,17], therefore, the problem of ray chaos is mainly important for long-range sound propagation.

During the past two decades, ray chaos in ocean acoustics has been an object of intense research, both theoretical and experimental [18–22]. Considerable attention has been paid to wave chaos [15,16,23–30]. The term *wave chaos* is related to wave-field manifestations of ray chaos. It was found that interference makes wave refraction more regular than anticipated from ray modeling, albeit the influence of ray chaos persists even for very low sound frequencies [31]. This problem becomes especially important in the light of the growing interest to hydroacoustical tomography, i.e., monitoring of the environment using sound signals. The classical scheme of tomography developed by Munk and Wunsch [32] is based on computation of eigenrays connecting the source and the receiver. It was shown in Ref. [33] that ray chaos leads to exponential proliferation of eigenrays with increasing distance. As a result, the inverse problem becomes ill posed, impeding environment reconstruction. However, wave-based corrections "stabilize" wave refraction, i.e., the standard semiclassical approximation typically overestimates ray chaos. Thus, one needs either an improved version of the semiclassical approximation for proper computation of eigenrays or some techniques for making implications about eigenray stability that rely on wave modeling, taking into account *a priori* the wave-based suppression of ray chaos. In the present paper we follow the latter approach.

As an example of the application of the method proposed here, we consider a realistic model of an acoustic waveguide in the Sea of Japan. Attention is concentrated on the track connecting the Gamov peninsula and Kita-Yamato bank. The length of the track is about 350 km. Our interest to this waveguide is motivated by unusually high stability of near-axial propagation, observed in the experiment conducted in 2006 [34]. Similar behavior was observed in an earlier experiment with a slightly different propagation track [35]. We carry out the statistical analysis of the FREO in order to explore the link between the stability of signal receptions in the experiments and the Lyapunov ray stability. It should be mentioned that regularity of near-axial propagation contradicts common expectations based on the experiments in the north Pacific Ocean [36–41] and numerical simulations with the canonical Munk waveguide [42].

The paper is organized as follows. The next section represents basic equations describing long-range sound propagation in the ocean. In Sec. III, we describe the waveguide used in the paper. Section IV introduces the FREO. Section V is devoted to the classical counterpart of the FREO, namely the one-step Poincaré map. In Sec. VI we demonstrate the approach for statistical analysis of FREO eigenfunctions. Statistics of FREO eigenvalues is considered in Sec. VII. In the conclusion we summarize and discuss the results obtained.

II. GENERAL EQUATIONS

Sound speed in the deep ocean typically has a minimum at some depth. This results in formation of a refractive waveguide, the so-called underwater sound channel, which prevents the contact of sound waves with the absorbing bottom. As sound absorption within a water column is fairly weak, an underwater sound channel enables sound propagation over distances of thousands kilometers. The largest distance had been achieved using explosive charges in the seminal experiment on sound transmission from Perth to Bermuda in 1960 [43,44].

The ocean is a layered media, and its horizontal variability is much weaker than the vertical one. This allows one to reduce the initial three-dimensional problem of wave propagation in an underwater sound channel to a two-dimensional one by assuming cylindrical symmetry and neglecting azimuthal coupling. Sound refraction is governed by spatial variability of sound speed

$$c(z,r) = c_0 + \Delta c(z) + \delta c(z,r), \tag{1}$$

where z is depth, r is the range coordinate, and c_0 is a reference sound speed. Sound-speed variations obey the double inequality

$$|\delta c|_{\max} \ll |\Delta c|_{\max} \ll c_0. \tag{2}$$

The left inequality implies that the range-dependent term can be treated as a weak perturbation of the background sound-speed profile. This term is mainly contributed from oceanic internal waves. The right inequality means that variations of the refractive index are weak, and only those waves which propagate at small angles with respect to the horizontal plane can avoid contact with the absorbing ocean bottom. Thus, one can invoke the small-angle approximation, in which an acoustic wave field is governed by the standard parabolic equation

$$\frac{i}{k_0}\frac{\partial \Phi}{\partial r} = -\frac{1}{2k_0^2}\frac{\partial^2 \Phi}{\partial z^2} + [U(z) + V(z,r)]\Phi, \tag{3}$$

where wave function Φ is related to acoustic pressure u by means of the formula $u = \Phi \exp(ik_0 r)/\sqrt{r}$. Here the denominator $\sqrt{r}$ responds for the cylindrical spreading of sound. Quantity k_0 is the reference wave number related to the sound frequency f as $k_0 = 2\pi f/c_0$. Functions $U(z)$ and $V(z,r)$ are determined by spatial sound-speed variations. In

the small-angle approximation they can be expressed as

$$U(z) = \frac{\Delta c(z)}{c_0}, \quad V(z,r) = \frac{\delta c(z,r)}{c_0}. \tag{4}$$

According to (2)

$$|V|_{\max} \ll |U|_{\max}, \tag{5}$$

that is, function $V(z,r)$ can be treated as a small perturbation. One can easily see that the substitution

$$k_0^{-1} \to \hbar, \quad r \to t \tag{6}$$

transforms the parabolic equation (3) into the Schrödinger equation for a particle with unit mass. This circumstance enables study of wave propagation using the approaches developed in quantum mechanics. In this relationship, function $U(z)$ serves as an unperturbed potential. As r is a timelike variable, $V(z,r)$ plays the role of a nonstationary perturbation.

In the short-wavelength limit $k_0 \to \infty$, solution of the parabolic equation (3) can be expressed as a sum of rays whose trajectories are governed by the Hamiltonian

$$H = \frac{p^2}{2} + U(z) + V(z,r), \tag{7}$$

where $p = \tan\chi$ and χ is the ray grazing angle (i.e., the angle with respect to the horizontal plane). The respective Hamiltonian equations read

$$\frac{dz}{dr} = \frac{\partial H}{\partial p} = p, \quad \frac{dp}{dr} = -\frac{\partial H}{\partial z} = -\frac{\partial U}{\partial z} - \frac{\partial V}{\partial z}. \tag{8}$$

Due to the analogy with classical mechanics, p is referred to as *ray momentum*.

III. MODEL OF A WAVEGUIDE

The model of the underwater sound channel in the Sea of Japan was elaborated using the hydrological data from the database [45]. Function $U(z)$ corresponding to the background sound-speed profile was approximated by the expression

$$U(z) = \begin{cases} U_1(z), & z \leqslant z_0 \\ U_2(z), & z > z_0 \end{cases}, \tag{9}$$

where

$$U_1(z) = \frac{c_1}{c_0} e^{-z/z_1}, \quad U_2(z) = \frac{c_1}{c_0} e^{-z_0/z_1} + \frac{g}{c_0}(z - z_0), \tag{10}$$

$c_0 = 1455$ m/s, $c_1 = 70$ m/s, $z_0 = 250$ m is the depth of the channel axis, i.e., the depth with the minimal sound speed, $z_1 = 30$ m, $g = 0.017$ s^{-1} (see Fig. 1). It is assumed that the ocean bottom is flat, and its depth h is 3 km. We consider only the deep-water propagation, albeit the source in the aforementioned experiments [34,35] was mounted into the bottom in the coastal zone near the Gamov peninsula. The shallow-water part of the waveguide was relatively short, less than 30 km, and did not have significant bottom features which could remarkably alter ray stability.

Expressions (9) and (10) permit analytical derivation of some basic model characteristics in the absence of horizontal inhomogeneity. In particular, ray cycle length, i.e., horizontal distance between two successive upper (or lower) ray turning

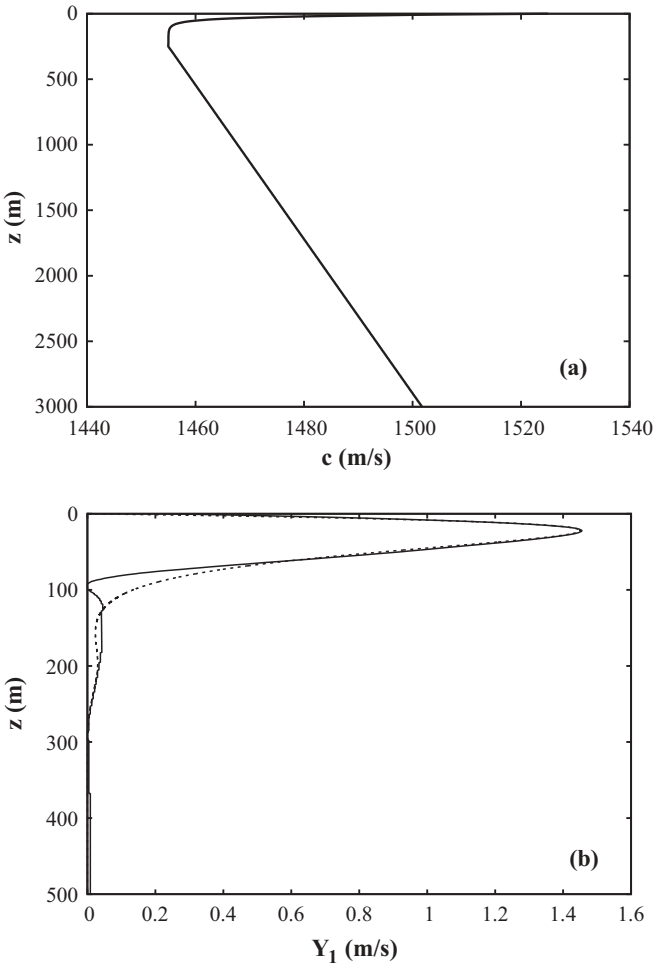

FIG. 1. (a) Unperturbed sound-speed profile, (b) the first empirical orthogonal function of the sound-speed perturbation (solid) and its smoothed approximation (dotted) used in ray calculations (see Appendices A and B for details).

points, can be determined as

$$D(E) = 2z_1\sqrt{\frac{2}{E}}\ln(\sqrt{\varepsilon} + \sqrt{\varepsilon - 1}) + \frac{2c_0\sqrt{2E_{\min}}}{g}\sqrt{\varepsilon - 1}, \tag{11}$$

where E is the analog of energy, determined as

$$E = \frac{p^2}{2} + U(z), \tag{12}$$

$\varepsilon = E/E_{\min}$, $E_{\min} = (c_1/c_0)\exp(-z_0/z_1)$. Ray cycle length is the analog of oscillation period in classical mechanics. Figure 2 represents dependence of ray cycle length on the initial ray momentum for the source located at the channel axis $z = 250$ m. Initial momentum p_0 depends on E as $p_0 = \pm\sqrt{2(E - E_{\min})}$. In a range-independent waveguide $D(-p_0) = D(p_0)$, therefore, we present in the figure only the branch corresponding to positive p_0. It should be mentioned that function $D(p_0)$ has two extrema in Fig. 2, the sharp maximum and the smooth minimum. The latter one can give rise to a so-called weakly divergent beam [46–49]. Its low divergence is associated with approximate equality of cycle length values for rays forming the beam. It will be

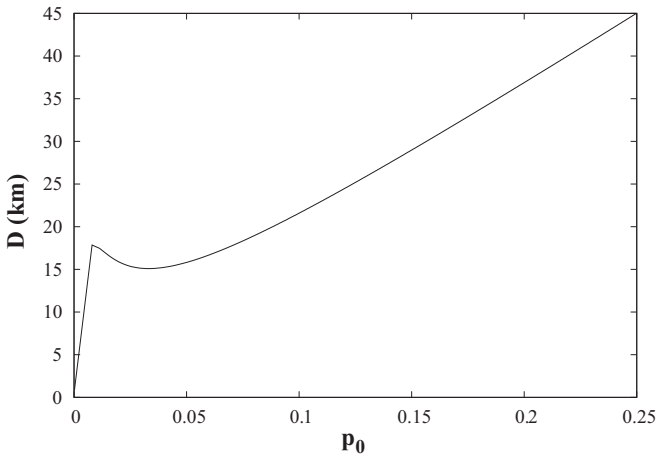

FIG. 2. Ray cycle length vs initial ray momentum for the source located at the channel axis.

demonstrated in Sec. V that the local minimum of $D(p_0)$ plays a significant role in ray stability.

In the present work we consider sound-speed perturbation solely contributed from oceanic internal waves. Processing the hydrological data for the Sea of Japan, it was found that the sound-speed perturbation can be fairly expressed as

$$V(z,r) = b_1(r)Y_1(z), \tag{13}$$

where $b_1(r)$ is a random function and $Y_1(z)$ is the first orthogonal empirical function depicted in Fig. 1(b). For simplicity, it is assumed that $b_1(r)$ is a stochastic process with the exponentially decaying autocorrelation function

$$\langle b_1(r)b_1(r')\rangle = \exp(-|r-r'|/\bar{r}), \tag{14}$$

where the correlation length $\bar{r}$ is taken to be 10 km, which is typical for the deep ocean [50]. The model of the sound-speed perturbation is described in detail in Appendix A.

IV. FINITE-RANGE EVOLUTION OPERATOR

The FREO had been introduced for studying wave propagation in a randomly inhomogeneous waveguide in Ref. [15]. Its quantum-mechanical analog was earlier considered in Ref. [14]. Basically, a FREO is an element of one-parameter group generated by the operator in the right-hand side of Eq. (3). Consider a solution $\Phi(z,r)$ of the parabolic equation (3) complemented with the standard boundary conditions

$$\Phi|_{z=0} = 0, \quad \left.\frac{d\Phi}{dz}\right|_{z=h} = 0 \tag{15}$$

and the initial condition $\Phi(z,r=0) = \bar{\Phi}(z)$, where $\bar{\Phi}(z)$ belongs to $L^2[0,h]$ and satisfies (15). The FREO $\hat{G}(\tau)$ then is defined on the subspace of $L^2[0,h]$ [restricted by (15)] as

$$\hat{G}(\tau)\bar{\Phi}(z) \equiv \Phi(z,r)|_{r=\tau}. \tag{16}$$

By definition, the FREO describes transformation of a wave field in the course of propagation along a finite waveguide segment of length τ. Each realization of inhomogeneity produces its own realization of the FREO. Our interest is concerned with statistical properties of the FREO and their connection to classical ray stability.

Note that the choice of the hard wall boundary condition at the bottom (15) is typical for the deep-ocean acoustics problems when the attention is restricted to the trapped modes, whose propagation is not affected by the bottom interaction. Under these conditions, no energy is absorbed by the bottom. Hence, if the attenuation in the sea water is negligible (this is true for the sound frequencies of our interest) and refraction index in (3) has no imaginary part, then the FREO is a unitary operator.

The FREO can be represented as a matrix in the basis of normal modes $\phi_n(z)$ satisfying the Sturm-Liouville problem

$$-\frac{1}{2k_0^2}\frac{\partial^2\phi_n(z)}{\partial z^2} + U(z)\phi_n(z) = E_n\phi_n(z) \tag{17}$$

with boundary conditions (15). Matrix elements of the FREO are given by

$$G_{mn}(\tau) = \int_0^h \phi_m(z)\hat{G}(\tau)\phi_n(z)\,dz. \tag{18}$$

Thus, the matrix elements G_{mn} are complex-valued amplitudes of modal transitions. For the range-independent waveguide, the matrix of FREO is diagonal with $|G_{mm}| = 1$.

Eigenvalues and eigenvectors of the FREO obey the equation

$$\hat{G}\Psi_m(z,r) = g_m\Psi_m(z,r). \tag{19}$$

Due to unitarity, eigenvalues g_m can be recast as

$$g_m = e^{-ik_0\epsilon_m}, \quad \epsilon_m \in \Re. \tag{20}$$

Since eigenvalues of the FREO belong to the unit circle in the complex plane, the FREO corresponds to the circular ensemble [51]. The FREO has much in common with the Floquet operator governing wave propagation in a range-periodic waveguide [25,27] and quantum dynamics in time-periodic systems. For instance, quantity ϵ_m is the analog of quasienergy in quantum mechanics.

Note that eigenvalues of $\hat{G}(\tau)$ may be easily computed using its matrix representation $G_{mn}(\tau)$. To accomplish this, one has to clip a finite block of this (infinite) matrix corresponding to the trapped modes, neglecting their interaction with high-order modes. This simplification is reasonable and does not affect accuracy of the eigenvalues computation (and the numerics confirms that) since the prevailing small-angle propagation corresponds to the low-order modes.

V. ONE-STEP POINCARÉ MAP

Chaos is a phenomenon with a classical origin, therefore, it is reasonable to consider the classical (i.e., ray-based) counterpart of the FREO. A finite-range (or finite-time) evolution operator can be thought of as a quantized one-step Poincaré map (this map is also referred to as the specific Poincaré map) [10]. An important advantage of the one-step Poincaré map is the opportunity to give a simple analytical description of the transition to chaos. The ray analog of the map is as follows [11]:

$$p_{i+1} = p(r=\tau|\,p_i,z_i), \quad z_{i+1} = z(r=\tau|\,p_i,z_i), \tag{21}$$

where $p(r=\tau|\,p_i,z_i)$ and $z(r=\tau|\,p_i,z_i)$ are the solutions of ray equations (8) with initial conditions $p(r=0)=p_i$, $z(r=0)=z_i$. Values of p and z, calculated at the i-th step of mapping become the initial conditions for the $(i+1)$-th step. This procedure is equivalent to the usual Poincaré map [52] for a range-periodic waveguide with the ray Hamiltonian

$$\bar{H}=\frac{p^2}{2}+U(z)+\tilde{V}(z,r). \tag{22}$$

Here $\tilde{V}(z,r)$ is periodic function in r,

$$\tilde{V}(z,r'+n\tau)=V(z,r'),\quad 0\leqslant r'\leqslant\tau \tag{23}$$

(here n is an integer). As it follows from (23), $\tilde{V}(z,r)$ is a sequence of identical pieces of $V(z,r)$, where each of them has the length τ. Thus, we replace the original randomly perturbed Hamiltonian system by an equivalent periodically perturbed one. This replacement is valid as long as we restrict ourselves by considering dynamics within the range interval $[0:\tau]$.

Due to the analogy with the usual Poincaré map, the main property of the one-step Poincaré map can be formulated as follows: *each point of a continuous closed ray trajectory of the map (21) corresponds to a starting point of the solution of (8), which remains stable in the Lyapunov sense until the range* $r=\tau$. The inverse statement is not, in general, true. Hence, the one-step Poincaré map provides a sufficient but not necessary criterion of stability. The main drawback of the one-step Poincaré map is that it typically underestimates the area of regular motion because the criterion of stability it relies on is very restrictive.

The basic properties of the map (21) can be described in terms of the theory of time-periodic Hamiltonian systems. To simplify the analysis of the ray equations, we apply the canonical transformation to the action-angle variables (I,ϑ). The ray action is determined by the formula

$$I=\frac{1}{\pi}\int_{z_{\min}}^{z_{\max}}\sqrt{2[E-U(z)]}\,dz, \tag{24}$$

where $z_{\min}$ and $z_{\max}$ are the upper and lower ray turning points, respectively, and E is determined by (12). The angle variable ϑ canonically conjugated to the action (24) is given by

$$\vartheta=\frac{\partial}{\partial I}\int_{z'}^{z}p\,dz, \tag{25}$$

where z' is one of the ray turning points. Ray action measures steepness of a ray trajectory and enters into the Einstein-Brillouin-Keller quantization rule

$$k_0 I_m=m-1/2,\quad m=1,2,\ldots, \tag{26}$$

establishing the link between normal modes of the unperturbed waveguide and satisfying the Sturm-Liouville problem [(15) and (17)] and modal rays. Here I_m is the action of a modal ray, and both ray turning points are assumed to be inside the water column, that is, rays undergo total internal reflection due to smooth vertical gradient of the refractive index $n=c_0/c(z,r)$.

The transformed ray Hamiltonian is written as

$$\bar{H}=H_0(I)+\tilde{V}(I,\vartheta,r). \tag{27}$$

Ray equations in terms of the new variables look in the following way:

$$\frac{dI}{dr}=-\frac{\partial H}{\partial\vartheta}=-\frac{\partial\tilde{V}}{\partial\vartheta},\quad \frac{d\vartheta}{dr}=\frac{\partial H}{\partial I}=\omega(I)+\frac{\partial\tilde{V}}{\partial I}, \tag{28}$$

where $\omega=2\pi/D$, D is ray cycle length (11).

Perturbation $\tilde{V}(I,\vartheta)$ can be expanded into a double Fourier series

$$\tilde{V}=\frac{1}{2}\sum_{k,k'=1}^{\infty}V_{k,k'}e^{i(k\vartheta-k'\Omega r)}+\text{c.c.}, \tag{29}$$

where $\Omega=2\pi/\tau$. Inserting (29) into (28), we obtain

$$\begin{aligned}\frac{dI}{dr}&=-\frac{i}{2}\sum_{k,k'=1}^{\infty}kV_{k,k'}e^{i(k\vartheta-k'\Omega r)}+\text{c.c.},\\ \frac{d\vartheta}{dr}&=\omega+\frac{1}{2}\sum_{k,k'=1}^{\infty}\frac{\partial V_{k,k'}}{\partial I}e^{i(k\vartheta-k'\Omega r)}+\text{c.c.}\end{aligned} \tag{30}$$

If the condition

$$k'D(I=I_{k,k'})=k\tau \tag{31}$$

is fulfilled, there occurs resonance in Eqs. (30). The pair of integers k' and k determines multiplicity of resonance $k{:}k'$. Resonances occur at certain values of the action $I_{k,k'}$, which correspond to the resonant tori. Ray dynamics in a small vicinity of a resonant torus corresponding to some pair (k,k') can be described using the resonance approximation [52], when one leaves only resonant terms in the right-hand side of (30). It should be mentioned that any resonant torus with multiplicity $k{:}k'$ simultaneously corresponds to an infinite number of resonances with multiplicities $(jk){:}(jk')$, where j is an integer. However, resonance Fourier amplitudes $V_{k,k'}$ rapidly decrease with increasing k and k'; therefore, only few low-order resonances influence significantly ray dynamics. Consequently, we can take into account only some finite number of dominant resonances. For further simplification, we employ the following procedures:

(1) As $\tilde{V}$ is a smooth function of z in the underwater sound channel considered, the derivative $d\tilde{V}/dI$ is small compared with ω, and the sum in the second equation of (30) can be dropped out.

(2) Near resonance, spatial frequency ω can be expanded as

$$\omega=\begin{cases}\omega(I_{k,k'})+\omega'_I\Delta I, & \omega'_I\neq 0\\ \omega(I_{k,k'})+\omega''_{II}\Delta I^2/2, & \omega'_I=0\end{cases}, \tag{32}$$

where $\omega'_I\equiv d\omega/dI$ and $\omega''_{II}\equiv d^2\omega/dI^2$. Here we assume that ω'_I and ω''_{II} do not vanish simultaneously.

The cases of $\omega'_I\neq 0$ and $\omega'_I=0$ correspond to nondegenerate and degenerate resonances, respectively. First, we consider the nondegenerate case. Introducing new variables,

$$\Delta I=I-I_{k,k'},\quad \psi=k\vartheta-k'\Omega r, \tag{33}$$

and expressing $V_{k,k'}$ as $|V_{k,k'}|\exp(i\zeta_{k,k'})$, we can rewrite (30) as

$$\frac{d(\Delta I)}{dr} = \sum_{l=1}^{L} lk|V_{lk,lk'}|\sin(l\psi + \zeta_{lk,lk'}) = -\frac{\partial \tilde{H}}{\partial \psi},$$
$$\frac{d\psi}{dr} = k\omega_I \Delta I = \frac{\partial \tilde{H}}{\partial(\Delta I)}, \tag{34}$$

where L is the number of dominant resonances and

$$\frac{\tilde{H}}{k} = \omega_I' \frac{(\Delta I)^2}{2} + \tilde{U}. \tag{35}$$

The potential part in the right-hand side of (35) is given by

$$\tilde{U} = \sum_{l=1}^{L} |V_{lk,lk'}|\cos(l\psi + \zeta_{lk,lk'}). \tag{36}$$

Maximal value of ΔI on the separatrix is determined by

$$\Delta I_{\max}^{k,k'} = 2\sqrt{\frac{\tilde{U}_{\max}}{|\omega_I'|}}, \tag{37}$$

where $\tilde{U}_{\max}$ is the absolute maximum of $\tilde{U}$. $\Delta I_{\max}^{k,k'}$ can be regarded as the half-width of the resonance k:k'.

If $L = 1$, then $\tilde{U}_{\max} = |V_{k,k'}|$, and $\tilde{H}$ turns into the universal Hamiltonian of nonlinear resonance [16,52]. In that case, the phase-space portrait of Eqs. (34) contains the domain of finite motion enclosed by the separatrix and corresponding to trapping into resonance. The terms with $l > 1$ may deform the pendulum-like phase-space portrait and, moreover, result in the presence of additional separatrices inside the domain of finite motion. The latter phenomenon can occur when the perturbation oscillates with depth [11].

In the degenerate case $\omega_I' = 0$ the Hamiltonian $\tilde{H}$ reads

$$\frac{\tilde{H}}{k} = \omega_{II}'' \frac{(\Delta I)^3}{6} + \tilde{U}, \tag{38}$$

and the resonance half-width is determined by the formula [53]

$$\Delta I_{\max}^{k,k'} = \left(\frac{12\tilde{U}_{\max}}{|\omega_{II}''|}\right)^{1/3}. \tag{39}$$

Transition to global chaos in the one-step Poincaré map happens when neighboring dominant resonances overlap. The criterion of overlapping is the well-known Chirikov criterion,

$$\frac{\Delta I_{\max}^{m,m'}(\tau) + \Delta I_{\max}^{n,n'}(\tau)}{\delta I(\tau)} \geqslant 1. \tag{40}$$

Here δI is the distance between neighboring dominant resonances m:m' and n:n' in the action space. Far enough from degenerate tori, variability of δI with τ for $\tau > D$ is described by the equation

$$\delta I(\tau) = \frac{2\pi}{\omega_I' \tau}, \tag{41}$$

that is, increasing of τ enhances resonance overlapping. However, the Chirikov criterion fails in the vicinities of degenerate resonances [54,55]. It is recognized that degenerate (or shearless) tori, corresponding to zeros of the derivative ω_I', can possess extraordinary persistence to chaos [53,56–59]. In underwater acoustics, shearless tori give rise to the so-called weakly divergent beams [46], i.e., the ray bundles with low geometrical divergence. In the model we consider, the derivative ω_I' has two isolated zeros corresponding to extrema of the function $D(p_0)$ depicted in Fig. 2. Both zeros correspond to almost horizontal rays with low values of the action, that is, there may be a small but long-living island of stability, whose evanescence cannot be described by means of the Chirikov criterion.

Differences in phase-space patterns corresponding to different realizations of the perturbation are associated with phase and amplitude fluctuations of Fourier amplitudes $V_{k,k'}$. However, the contribution of these fluctuations is limited, therefore, the ratio of the phase-space volumes corresponding to regular and chaotic motion is mainly controlled by τ and weakly varies from one realization to another (see below for an illustration). This property allows one to consider the one-step Poincaré map as a useful tool for studying randomly driven dynamical systems of various physical origins [11–13].

The above expectations are confirmed by computations of phase portraits via the one-step Poincaré map. Figure 3 illustrates phase-space portraits corresponding to three different realizations of the sound-speed perturbation. Each of the phase-space portraits represents a mixed phase-space structure consisting of regular and chaotic domains. Phase portraits with the same τ mainly differ only in angular locations of regular islands, whereas their overall structure is very similar. The main regular domain is placed near the point $z = z_0$, $p = 0$ and corresponds to flat rays intersecting the horizontal plane with the smallest angles. Resonance overlapping is enhanced as τ grows, and stable islands eventually submerge into the chaotic sea. However, a small region of stability near $z = z_0$, $p = 0$ survives for distances of hundreds of kilometers, transforming into a chain of islands. This chain corresponds to the smooth minimum of the function $D(p_0)$ (see Fig. 2), i.e., it corresponds to a weakly divergent beam that maintains stability. Hence, formation of a persistent weakly divergent beam can be considered as a possible mechanism responsible for unusual stability of near-axial rays, observed in experiments [34,35].

It should be emphasized that stability of flat rays is not typical for sound propagation in the deep ocean. Numerous experiments on long-range sound propagation in the northeastern Pacific Ocean (see, for instance, Refs. [36–40]) indicate on strong irregularity of flat near-axial rays, associated with ray chaos [17,60]. The "deterministic" mechanism of near-axial chaos is ray scattering on vertical resonances caused by small-scale depth oscillations of the sound-speed perturbation [27,29,31]. These oscillations result from higher modes of an internal-wave field. In the Sea of Japan, the contribution of the higher modes is weak, therefore, the sound-speed perturbation can be fairly described by Eq. (13), where depth dependence is given by a smooth function $Y_1(z)$. This means that there is no scattering on vertical resonances in the waveguide considered, and we observe a qualitatively different scenario of ray chaos, associated with overlapping of nonlinear ray-medium resonances (31). It should be noted that weakness of higher internal-wave modes is a peculiar feature of the Sea of Japan, caused by the specific form of the buoyancy frequency profile.

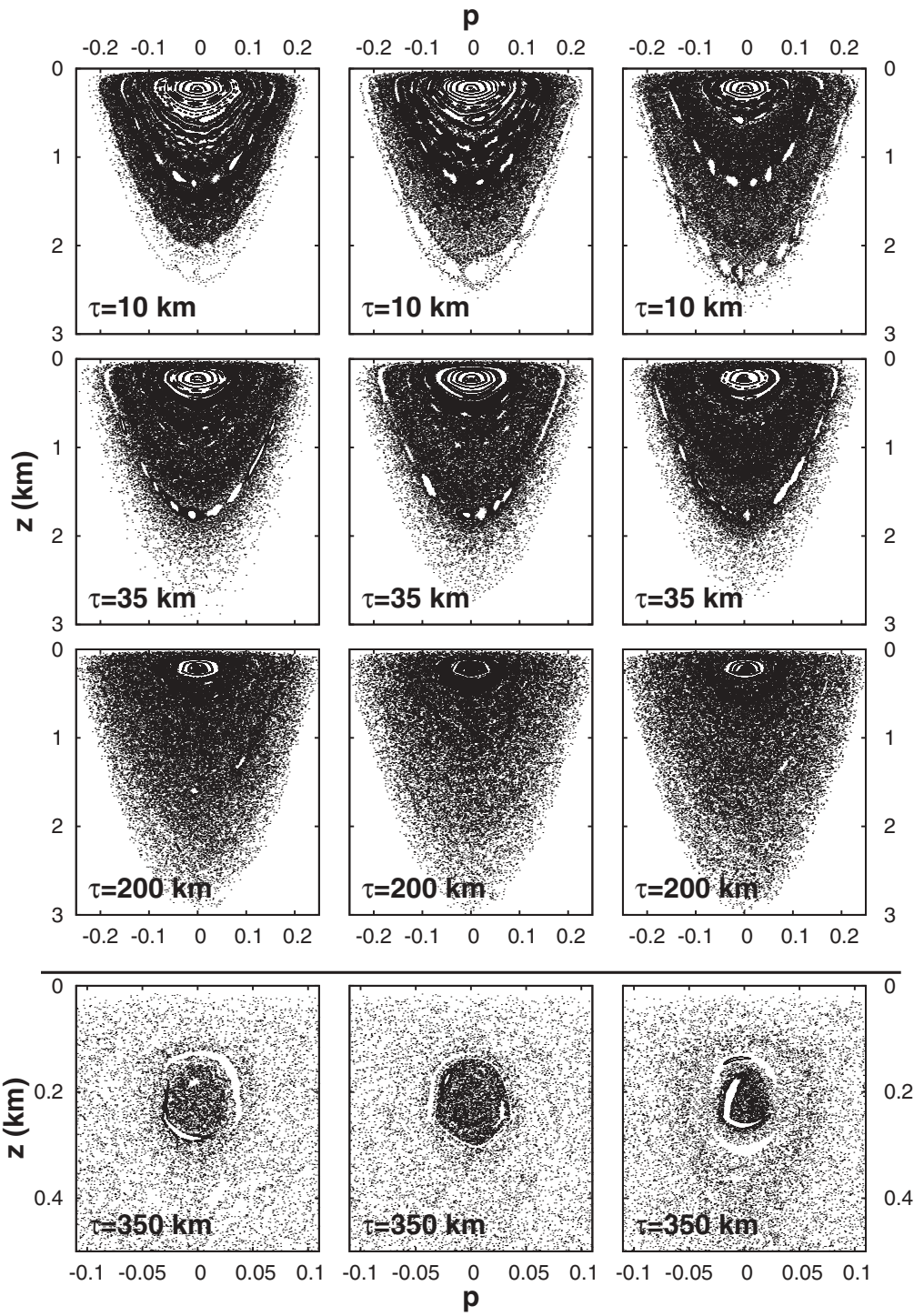

FIG. 3. Ray phase-space portraits constructed via the one-step Poincaré map (21). Each column corresponds a single realization of the sound-speed perturbation. Value of τ is indicated in the left lower corner.

VI. EIGENFUNCTION STATISTICS

As shown in the preceding section, phase space of ray equations in a randomly inhomogeneous waveguide may contain domains of finite-range stability. On a wave level, information about such domains is hidden in subtle correlations between neighboring elements in the matrix of the FREO. Indeed, efficient description of a random system anyway requires statistical approach. However, simple averaging of the FREO matrix should smooth out the traces of regular domains. According to the results of ray modeling, regular domains in oceanic waveguides can persist over ranges of hundreds kilometers and, therefore, their influence has to be taken into account. This problem can be resolved when one performs statistical sampling over realizations of FREO eigenfunctions. In this case, the information about regular domains is stored

by certain eigenfunctions which can be identified according to some criteria.

There are many ways to identify of "regular" or "chaotic" eigenfunctions (see, for instance, Refs. [61,62]). In the present work we use only one of them, which seems to be convenient for the statistical analysis. Each eigenfunction can be expressed as a superposition of normal modes as follows:

$$\Phi_m(z) = \sum_n c_{mn}\phi_n(z), \tag{42}$$

where c_{mn} is the m-th component of n-th eigenvector of the matrix $\hat{G}$, $\phi_n(z)$ is the n-th normal mode. Ray chaos corresponds to intense energy exchange between normal modes [23,29,42]; therefore, a "chaotic" eigenfunction is a compound of many modes. The stronger the chaos, the larger the number of contributing modes. Hence, we can characterize "chaoticity" by estimating participation ratio (PR) in the expansion (42) [63]. The PR of the n-th eigenfunction is calculated as

$$\nu = \left(\sum_{m=1}^{M} |c_{mn}|^4\right)^{-1}, \tag{43}$$

where M is the number of trapped modes. The PR is equal to 1 in an unperturbed waveguide and grows as scattering intensifies.

Analysis of eigenfunctions has some advantages over the analysis of eigenvalues. The main advantage is the possibility to associate each eigenfunction with some set of normal modes and, thereby, associate it with a certain geometry of propagation. To facilitate this association, we can use the parameter μ [25] defined as

$$\mu = \sum_{m=1}^{M} |c_{mn}|^2 m. \tag{44}$$

In an unperturbed waveguide, only one normal mode contributes to each eigenfunction, and μ coincides with the number of this mode.

Taking into account the quantization rule (26), we obtain the formula

$$\langle I \rangle = \frac{\mu}{k_0} + \frac{1}{2k_0}, \tag{45}$$

which gives the mean action corresponding to an eigenfunction. According to (45), the parameter μ determines the phase-space location of the eigenfunction and can serve as its identificator. Figures 4 and 5 illustrate eigenfunction distributions in the μ-ν plane, where ν is the PR (43) for the frequencies 500 and 100 Hz, respectively.

Let us, first, consider Fig. 4, corresponding to the frequency of 500 Hz. Energy transfer between different modes is relatively weak for small values of τ, therefore, the distribution is mainly concentrated near $\nu = 1$. We want to focus attention on the dense spots elongated in the ν direction. They correspond to eigenfunctions reflecting mode-medium resonance [23] being the wave counterpart of the ray-medium resonance (31) and mathematical analog of the quantum nonlinear resonance [64]. Indeed, an isolated ray-medium resonance produces oscillations of ray action inside the interval $I_0 - \Delta I_{\max} \leqslant I \leqslant I_0 + \Delta I_{\max}$, where I_0 is a resonance

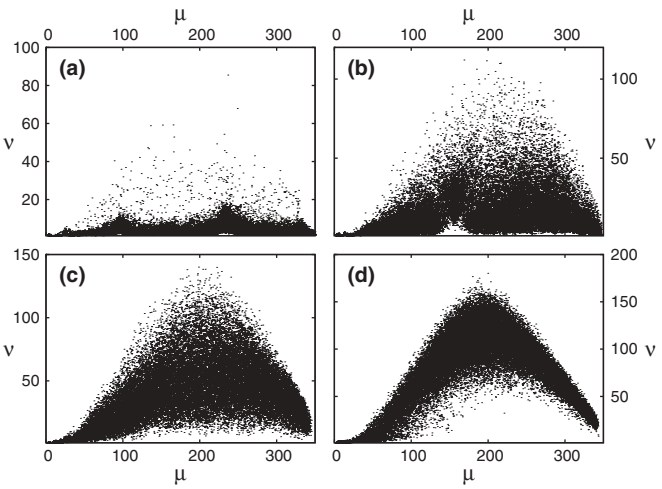

FIG. 4. Distribution of eigenfunctions in the μ-ν plane, where the parameter μ is given by (44) and ν is the participation ratio (43). Distance values: (a) $\tau = 10$ km, (b) $\tau = 35$ km, (c) $\tau = 100$ km, (d) $\tau = 350$ km. The sound frequency is 500 Hz.

action and $\Delta I_{\max}$ is resonance width in the action space. In the case of nondegenerate ray-medium resonance, $\Delta I_{\max}$ is determined by (37). According to the principle of ray-mode duality, these oscillations of action correspond to coherent transitions between the normal modes whose numbers satisfy the inequality

$$m_0 - \Delta m \leqslant m \leqslant m_0 + \Delta m, \tag{46}$$

where $m_0 = k_0 I_0 + 1/2$, $\Delta m = k_0 \Delta I_{\max}$. Resonance-induced modal transitions give rise to eigenfunctions with $\mu \simeq m_0$ and ν varying from 1 to Δm. As long as resonance values of the action, being determined by τ, are the same for all realizations of the perturbation, these eigenfunctions form vertically elongated concentrations of points (hereafter we shall refer to them as "stripes") in the μ-ν plane. Location of mode-medium resonances along the μ axis can be found

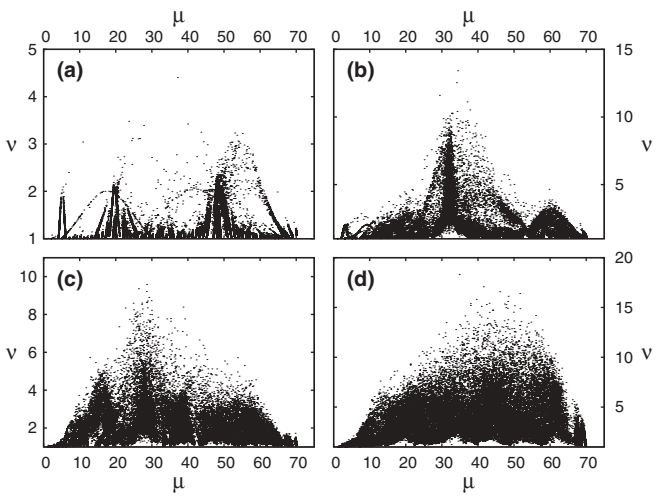

FIG. 5. The same as described in the caption to Fig. 4 but for the frequency of 100 Hz. (a) $\tau = 10$ km, (b) $\tau = 35$ km, (c) $\tau = 100$ km, and (d) $\tau = 350$ km.

using the formula

$$k'D(I = \langle I \rangle) = k\tau, \tag{47}$$

where $\langle I \rangle$ is linked to μ by (45). For instance, the left stripe in Fig. 4(a) corresponds to $D = 30$ km and the resonance 3:1, the right one corresponds to $D = 40$ km and resonance the 4:1, and the unique resolved stripe in Fig. 4(b) corresponds to $D = 35$ km and the resonance 1:1.

Stripes induced by mode-medium resonance disappear with increasing τ due to overlapping of mode-medium resonances and delocalization [23,64]. Delocalization leads to abrupt growth of PR. It eventually subjects all eigenfunctions in the interval between $\mu \simeq 100$ and $\mu \simeq 300$, resulting in the "boomerang" pattern in the μ-ν plane, as illustrated in Fig. 4(d). The left and right ends of the "boomerang" are formed by weakly scattered eigenfunctions. The left end corresponds to the almost horizontal near-axial propagation, that is, its regularity can be associated with long-living stable islands in the one-step Poincaré map.

Eigenfunction distribution in the μ-ν plane for the frequency of 100 Hz has a more complicated structure. It is exceptionally regular for $\tau = 10$ km and $\tau = 35$ km, as shown in Figs. 5(a) and 5(b). Mode-medium resonances reveal themselves as "stalagmites." Each stalagmite is drawn by a family of distinct weakly biased vertical lines. Contours of the most pronounced stalagmite for $\tau = 35$ km, corresponding to the resonance 1:1, are somewhat disordered and smeared.

It should be emphasized that some traces of stalagmite-like patterns survive, even for distances of hundreds kilometers, despite global overlapping of ray-medium resonances. Persistence of stalagmites for large τ indicates on the presence of eigenstates localized near periodic orbits of the one-step Poincaré map. It can be thought of as the suppression of delocalization associated with overlapping of mode-medium resonances, that is, global ray chaos due to resonance overlapping is not reflected in wave patterns. The most likely mechanism responsible for the suppression of delocalization and recovery of stalagmites is the dynamical localization [51,65], when destructive interference limits wave-packet diffusion in phase space. Dynamical localization can be considered an analog of Anderson localization. Recovery of stability in the vicinities of overlapped ray-medium resonances had been earlier reported in Ref. [27] for range-periodic waveguides.

Besides stalagmites, Figs. 5(a) and 5(b) illustrate the patterns in the form of "bridges." For instance, a pronounced "bridge" in the left part of Fig. 5(a) connects the points $\mu = 5$, $\nu = 1$ and $\mu = 30$, $\nu = 1$. The eigenfunctions producing the "bridges" consist of normal modes satisfying the condition

$$k_0(E_m - E_n) = \frac{2\pi l}{\tau}, \quad m > n. \tag{48}$$

The aforementioned "bridge" in Fig. 5(a) satisfies (48) with $m = 30$, $n = 5$, and $l = 9$. Condition (48) is equivalent to quantum resonance between two energy levels. Bridges appear when resonance (48) is well isolated, i.e., the modes m and n are not coupled with other modes. The formation of bridges is described in Appendix C. Isolation of resonance (48) becomes violated with increasing τ, therefore, the correlation between ν and μ ceases, and ordered "bridges" transform into disordered clouds of points.

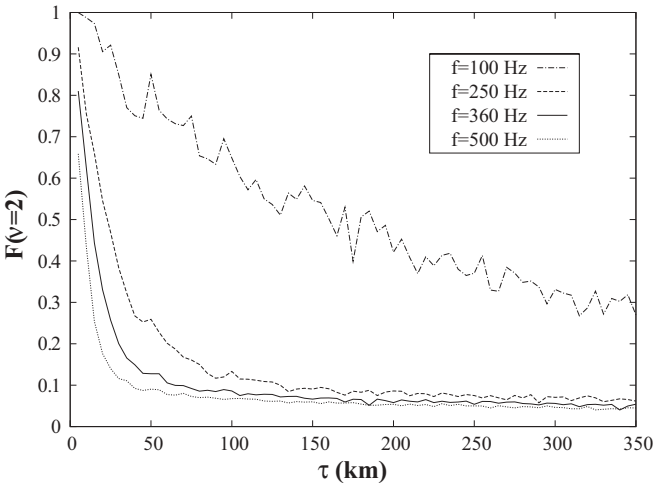

FIG. 6. Fraction of strongly localized eigenfunctions as function of distance. The criterion of strong localization is the inequality $\nu \leqslant 2$.

In practice, it is useful to know the fraction of the eigenfunction ensemble corresponding to regular propagation. Taking into account the correspondence between rays and modes established by the WKB theory (26), this quantity can be regarded as some analog of regular phase-space volume v_r considered in the preceding section. It can be estimated by means of the cumulative distribution function

$$F(\nu) = \int_1^{\nu} \rho(\nu')\, d\nu', \tag{49}$$

where $\rho(\nu')$ is the probability density function of ν. We can conditionally distinguish two regimes of localization: strong localization and moderate localization. Strong localization implies that the eigenfunction of FREO is close to one of normal modes of the unperturbed waveguide. To select strongly localized eigenfunctions, we can use the inequality $\nu \leqslant 2$. Dependence of $F(2)$ on the horizontal distance τ is depicted in Fig. 6. Evidently, the fraction of strongly localized eigenfunctions is much larger for $f = 100$ Hz than for higher frequencies. The curves corresponding to the higher frequencies are close to each other. They drop down in the range of small τ and then the decrease of $F(2)$ becomes powerlike and very slow. The heavy tail in the dependence of $F(2)$ on τ is linked to the presence of the long-living islands of stability in the neighborhood of the weakly divergent beam; otherwise one would expect $F(2)$ to vanish rapidly. Markedly, the fraction of eigenfunctions with strong localization is larger and decays much more slowly than it is anticipated by classical ray calculations via the one-step Poincaré map. This can indicate the significance of wave-based effects like the dynamical localization, as well as violation of the Chirikov criterion in the presence of shearless tori.

In the regime of moderate localization, mode coupling can be sufficiently strong, but an eigenfunction occupies relatively small phase-space volume, that is, the PR is limited. We use the inequality $\nu \leqslant 0.1M$ as the criterion of moderate localization. As demonstrated in Fig. 7, almost all eigenfunctions corresponding to the frequency of 100 Hz are moderately localized.

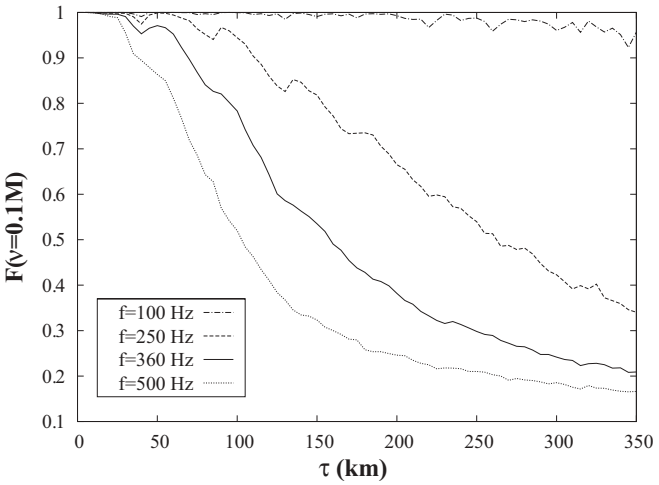

FIG. 7. Fraction of moderately localized eigenfunctions vs distance. The criterion of moderate localization is the inequality $\nu \leqslant 0.1M$, where M is the number of trapped modes.

It indicates the confinement of chaos-assisted diffusion due to dynamical localization. For higher frequencies, the impact of dynamical localization is weaker, and the fraction of moderately localized eigenfunctions significantly decreases with τ.

VII. LEVEL-SPACING STATISTICS

It was long ago recognized that wave chaos reveals itself in the statistics of level spacings. A level spacing is defined as

$$s = \frac{k_0 M(\epsilon_{m+1} - \epsilon_m)}{2\pi}, \quad m = 1,2,\ldots,M, \quad \epsilon_{M+1} = \epsilon_1 + \frac{2\pi}{k_0}, \tag{50}$$

where ϵ_m increases with increasing m and M is the total number of eigenvalues for a single realization of the FREO, equal to the number of trapped modes.

Level-spacing statistics can be studied in terms of the random matrix theory [51]. Regular dynamics implies that the matrix of the FREO consists of separate independent blocks. In this case, level sequences from different blocks are statistically independent, therefore, the resulting level-spacing distribution obeys the Poisson law,

$$\rho(s) \sim \exp(-s). \tag{51}$$

Under conditions of ergodic chaos, all normal modes are coupled to each other. This results in repulsion of neighboring levels, and this phenomenon is closely related to spectral splittings induced by tunneling [66]. In this case, level-spacing statistics is described by the Wigner surmise

$$\rho(s) \sim s^{\zeta} \exp(-Cs^2), \tag{52}$$

where constants ζ and C depend on symmetries of the FREO. As the FREO does not possess the symmetry $r \to -r$, it corresponds to the circular unitary ensemble (CUE) with $\zeta = 2$ and $C = 4/\pi$ [14].

The most interesting case is a mixed phase space, with the coexistence of regular and chaotic domains. Level-spacing statistics then should be described by some combination of Poisson and Wigner laws. In the short-wavelength limit one can use the Berry-Robnik distribution [67]

$$\rho(s) = \left[v_r^2 \operatorname{erfc}\left(\frac{\sqrt{\pi}}{2} v_c s\right) + \left(2v_r v_c + \frac{\pi}{2} v_c^3 s\right) \times \exp\left(-\frac{\pi}{4} v_c^2 s^2\right)\right] \exp(-v_r s), \tag{53}$$

where v_r and v_c are relative phase-space volumes corresponding to regular and chaotic ray motion, respectively, $v_r + v_c = 1$. In (53), it is assumed that the phase space consists of only two distinct domains: one regular and one chaotic. In the limiting cases $v_r = 1$ and $v_c = 1$, the Berry-Robnik formula (53) reduces to the Poisson distribution and the Wigner distribution for the orthogonal ensemble ($\zeta = 1$), respectively. The Berry-Robnik distribution undergoes a smooth transition from the Poisson law to the Wigner law as v_r decreases from 1 to 0. It should be taken into account that Wigner distributions for orthogonal ($\zeta = 1$) and unitary ($\zeta = 2$) ensembles are not identical; they are roughly similar, though. Therefore, one can use (53) only as some rough approximation for the circular unitary ensemble. This is not a unique shortcoming of the analysis via formula (53); the Berry-Robnik distribution is based on the assumption of the total statistical independence of the matrix blocks corresponding to regular and chaotic dynamics. This assumption is completely fulfilled only in the semiclassical limit. As wave corrections grow, independence degrades due to regular-to-chaotic tunneling [68]. Hence, the Berry-Robnik formula cannot work perfectly for low-frequency sound propagation.

Another problem arises when perturbation of the waveguide oscillates quickly with depth [15]. On the ray level, these oscillations lead to strong chaos accompanied by extensive splittings of periodic orbits of the map (21) due to bifurcations. Due to the link between periodic orbits and energy spectra, cascades of bifurcations give rise to clusters of nearly degenerate levels. Under these conditions, level-spacing statistics does not obey universality conjecture [69], and the Berry-Robnik formula becomes inapplicable. The applicability can be partially recovered with increasing wavelength, when contributions of individual orbits within a cluster interfere, and level splitting is suppressed [15,27]. Fortunately, the Sea of Japan is a rare example of an oceanic environment where sound-speed perturbation does not exhibit fast depth oscillations due to a specific hydrological structure, and the impact of ray bifurcations is relatively weak.

Function (53) should describe level-spacing statistics for single realizations of the FREO. Very unfortunately, this is problematic because one encounters insufficiency of the statistical ensemble. Indeed, long-range sound propagation is feasible only with low acoustic frequencies of tens or hundreds of hertz. In this frequency range, number of trapped modes does not exceed several hundreds of hertz. To resolve this problem, we consider the ensemble-averaged level-spacing distribution

$$\rho(s,\tau) = \lim_{N\to\infty} \frac{1}{N} \sum_{n=1}^{N} P_n(s,\tau), \tag{54}$$

where $P_n(s,\tau)$ is a level-spacing distribution corresponding to the n-th realization of FREO. Fitting the function $\rho(s,\tau)$

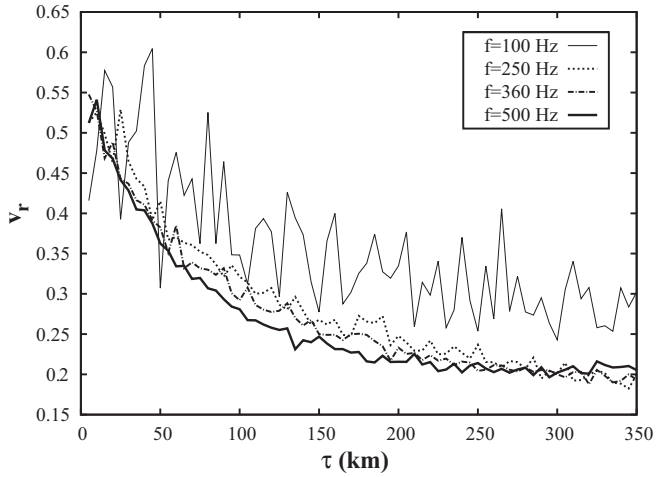

FIG. 8. Fraction of the phase-space volume corresponding to regular motion vs distance τ for various frequencies.

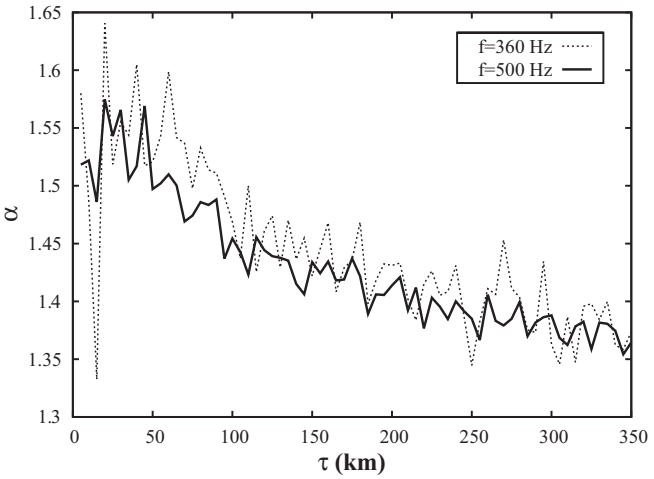

FIG. 9. Relano parameter α vs distance τ.

with the Berry-Robnik distribution (53), one can estimate the number of regularly propagating modes for various values of τ and thereby track the transition to chaos with increasing τ. However, it should be noted that formula (54) enables accurate estimate of v_r only if fluctuations of v_r are weak; otherwise, one should take into account nonlinearity of ρ as a function of v_r in (53).

We calculated the ensemble-averaged level-spacing distribution $\rho(s,\tau)$ using the formula (54) and fitted it, for each value of τ, by means of the Berry-Robnik distribution (53). Thus, we obtained dependence of the regular phase-space volume v_r on distance τ. As is shown in Fig. 8, v_r rapidly decreases in the first 100–150 km, reflecting the shrinking of the regular domains due to overlapping of classical resonances. It then becomes almost constant. This may indicate the influence of the long-living stable islands in the vicinity of the weakly divergent beam. Notably, the curves corresponding to 250, 360, and 500 Hz are very close to each other, whereas the curve corresponding to 100 Hz lies above them and undergoes strong fluctuations which persist even with increasing number of realizations. It should be mentioned that the above estimates of v_r have limited accuracy because the assumptions underlying the formula (53) are satisfied only approximately. Therefore, the results obtained using the Berry-Robnik distribution are rather qualitative than quantitative, especially for low sound frequencies.

In addition, we used the method of spectral analysis, developed by A. Relano and coworkers in Ref. [70]. In this method, one, first, constructs a series

$$\delta_n = \sum_{i=1}^{n} (s_i - \langle s \rangle), \tag{55}$$

where $n = 1,2,\ldots,N-1$, and N is the total number of eigenvalues. Then, making a discrete Fourier transform,

$$\bar{\delta}_k = \frac{1}{\sqrt{N}} \sum_n \delta_n \exp\left(\frac{2\pi i k n}{N}\right), \tag{56}$$

one finds the power spectrum

$$S(k) = |\bar{\delta}_k|^2. \tag{57}$$

Generally, an ensemble-averaged spectrum obeys a power law,

$$\langle S(k) \rangle \sim k^{-\alpha}. \tag{58}$$

Relano and coworkers found that regular dynamics corresponds to $\alpha = 2$, and global chaos results in $\alpha = 1$. In the mixed regime, α takes on an intermediate value between 1 and 2 [71]. Figure 9 demonstrates that α decreases with increasing τ for the frequencies of 360 and 500 Hz, indicating gradual transition to chaos. However, α varies relatively slowly and remains near the middle value 1.5 for all distances considered, despite the marked changes in the classical phase-space portrait (see Fig. 3). Analogous dependencies for the frequencies of 100 and 250 Hz exhibit strong fluctuations and, therefore, are not presented in the figure. This implies that the method developed in Refs. [70,71] provides good agreement only for relatively short wavelengths which are not relevant for long-range sound propagation.

VIII. CONCLUSION

In the present paper we examine the influence of finite-range ray stability on wave dynamics in a randomly inhomogeneous waveguide by means of the quasideterministic approach, involving resonances, periodic orbits, phase-space portraits, and so on. Our approach is based on spectral analysis of the finite-range evolution operator. We utilize various methods of spectral analysis and compare the results obtained. For instance, we consider distribution of eigenfunctions in the μ-ν space and approximate level-spacing statistics by means of the Berry-Robnik distribution and study eigenvalues series using the method developed by A. Relano and coworkers [70,71]. Comparing the results obtained with different methods, we conclude that the method based on eigenfunction analysis is the most favorable method. Its important advantage is the possibility to study separately scattering of different modes of a waveguide and find out the modes corresponding to regular propagation. A detailed view of the eigenfunction distribution in the μ-ν space suggests that the mechanism of the chaos onset with increasing distance can be associated with overlapping and delocalization of mode-medium resonances. The approach

based on the statistical analysis of level spacings by means of the Berry-Robnik formula gives a qualitative description of the transition but does not ensure quantitative agreement. The Relano method also gives the qualitative description but cannot make any quantitative estimates due to its semiempirical nature.

We consider the underwater sound channel in the Sea of Japan as an example. Our analysis shows that almost horizontal near-axial sound propagation preserves regularity over distances of hundreds kilometers. There are two factors responsible for near-axial stability. The first factor is the peculiar hydrological structure in the region considered, resulting in the absence of vertical oscillations of the sound-speed perturbation. This circumstance leads to a qualitatively different scenario of ray chaos, as compared with the well-known acoustic experiments in the northeastern Pacific Ocean [36–40]. The second factor is the formation of the weakly divergent beam supported by long-living stable islands in classical phase space. A weakly divergent beam occurs in the vicinity of the shearless torus. Nondispersive motion of quantum wave packets near shearless tori was observed in Refs. [54,72]. In the present paper we show that shearless tori can enhance wave coherence, even in the presence of random inhomogeneity, and result in powerlike decreasing of the fraction of regular eigenfunctions.

It should be mentioned that the classical description by means of the one-step Poincaré map plays an important role our approach. Although the one-step Poincaré map does not yield accurate quantitative estimates for low-frequency sound propagation, it provides a classical interpretation of basic FREO spectral properties. For example, the stripes and "stalagmites" in Figs. 4 and 5 are directly linked to resonances of the map. In fact, we can consider the FREO as the quantized one-step Poincaré map, and this analogy implies a deterministic scenario of transition to chaos in randomly inhomogeneous waveguides, associated with overlapping of classical resonances and corresponding delocalization of their wave-based counterparts. From this viewpoint, it is noteworthy to focus attention on the recovery of "stalagmites" with decreasing sound frequency. This phenomenon corresponds to localization of eigenfunctions in the vicinities of classical resonances which are completely overlapped in the ray limit. Recovery of stalagmites can be considered as a specific manifestation of dynamical localization. It infers that low-frequency waves in randomly inhomogeneous waveguides can exhibit intermittent behavior instead of diffusive spreading.

We suppose that applicability of the approach presented in this paper is not limited to problems of wave propagation in random media. An analog of the FREO can be readily used for studying of noise-induced quantum transport and related phenomena. We suggest that a combination of deterministic and statistical approaches should provide an insightful view on details of dynamics, especially in the presence of intermittency or synchronization.

ACKNOWLEDGMENTS

This work was supported by the Russian Foundation of Basic Research (projects 09-05-98608, 12-05-33022, and 12-02-31416), the Federal Program "World Ocean," and the "Dynasty" Foundation. Authors are grateful to A. R. Kolovsky, S. Tomsovic, O. A. Godin, K. V. Koshel and V. V. Novotryasov for helpful comments concerning the subject of the research.

APPENDIX A: SOUND-SPEED PERTURBATION

The model of the internal-wave-induced sound-speed perturbation was built up in several steps. First, we computed the range-averaged profile of buoyancy frequency, using the hydrological data [45]. We then calculated realizations of the sound-speed perturbation using the method proposed in Ref. [73]. In order to facilitate numerical simulation, the perturbation was expanded over empirical orthogonal functions [74]

$$\delta c(z,r) = \langle \delta c(z) \rangle + \sum_n b_n(r) Y_n(z). \tag{A1}$$

Empirical orthogonal functions $Y_n(z)$ are the eigenvectors of the covariance matrix $\hat{K}$ with elements

$$K_{ij} = \frac{1}{L} \sum_{l=1}^{L} [\delta c_l(z_i) - \langle \delta c(z_i) \rangle][\delta c_l(z_j) - \langle \delta c(z_j) \rangle], \tag{A2}$$

where index l numbers L statistically independent realizations of $\delta c(z)$, $\{z_i\}$ is a vector of depth values, and the angular brackets denote ensemble average. As δc is caused by internal waves, one can set $\langle \delta c \rangle = 0$. Eigenvalues of the matrix $\hat{K}$ quantify contributions from the corresponding eigenvectors in the expansion (A1). It was found that the contribution of the first orthogonal function prevails (about 70%), and one can fairly represent the sound-speed perturbation as the product (13).

Realizations of $b_1(r)$ can be computed via the formula $b_1 = \sqrt{2\bar{r}}\eta$, where η is a solution of the Ornstein-Uhlenbeck stochastic differential equation in the Stratonovich sense,

$$\frac{d\eta}{dr} = -\frac{1}{\bar{r}}\eta(r) + \frac{1}{\bar{r}}\xi(r). \tag{A3}$$

The method of numerical solution of this equation is described, for instance, in Ref. [75]. Here ξ is a Gaussian white noise satisfying

$$\langle \xi(r) \rangle = 0, \quad \langle \xi(r)\xi(r') \rangle = \delta(r - r'). \tag{A4}$$

The resulting function $b_1(r)$ satisfies $\langle b_1^2(r) \rangle \simeq 1$.

APPENDIX B: SOME REMARKS ON NUMERICAL SIMULATION

In ray calculations, the jump of the derivative dU/dz at $z = z_0$ leads to fast growth of numerical error. Therefore, we replaced the expression (9) for $U(z)$ by the smoothed function

$$U(z) = U_1(z) + \frac{1}{2}\left[1 + \tanh\frac{z - z_0}{\Delta}\right] U_2(z), \tag{B1}$$

where $\Delta = 1$ m.

The first empirical orthogonal function of the perturbation $Y_1(z)$ involves steplike changes in the depth interval from 100 to 300 m. These changes are caused by the depth discretization of the hydrological data and physically irrelevant. Wave modeling is insensitive to them, but ray-based calculations can be significantly affected. Therefore, ray calculations were carried out with the smoothed first empirical orthogonal

function given by

$$Y_1 = A y_a \exp\left(-y_a^n\right) + B \exp\left(-y_b^2\right), \quad \text{(B2)}$$

where $A = 0.0027$, $y_a = z/z_a$, $n = 1.1$, $z_a = 24$ m, $B = 2 \times 10^{-5}$, $y_b = (z - z_c)/z_b$, $z_b = 50$ m, $z_c = 200$ m.

Each realization of the FREO is represented as a matrix in the basis of normal modes being solutions of the Sturm-Liouville problem (17) with the boundary conditions (15). Only purely water modes which propagate without reaching the bottom are taken into account. They are selected using the criterion $E_m < U(z = h)$, where E_m is the m-th eigenvalue of the Sturm-Liouville problem (17). This criterion ensues from the WKB approximation for normal modes [23]. Number of trapped modes M depends on sound frequency. It is equal to 72 for $f = 100$ Hz, 179 for $f = 250$ Hz, 259 for $f = 360$ Hz, and 361 for $f = 500$ Hz. Statistical ensembles of the FREOs, corresponding to the frequencies of 250, 360, and 500 Hz, are calculated with 100 realizations of the perturbation. The ensemble corresponding to 100 Hz is calculated with 500 realizations. For each realization, we construct a family of the FREOs $\hat{G}(\tau)$, where $\tau = 5, 10, 15, \ldots, 350$ km.

APPENDIX C: BRIDGELIKE PATTERNS

Each realization of the FREO can yield eigenfunctions manifesting resonance (48). If resonance (48) corresponding to some numbers (l, m, n) is localized, i.e., the modes m and n are not affected by other resonances, then the respective eigenfunction is a superposition of normal modes m and n,

$$\Phi_{\text{res}}(z) \simeq c_m \phi_m + c_n \phi_n, \quad |c_m|^2 + |c_n|^2 \simeq 1. \quad \text{(C1)}$$

As this takes place, the ratio of amplitudes $|c_m|/|c_n|$ is determined by the phase of the resonance harmonics of the perturbation. For the perturbation (13), the complex-valued amplitude of the l-th resonance harmonics reads

$$B_l = \frac{1}{\tau} \int_0^\tau b_1(r) \exp\left(-i \frac{2\pi l r}{\tau}\right) dr. \quad \text{(C2)}$$

The phase of the resonance harmonics is a random quantity with a uniform probability density in the range $[0 : 2\pi]$. Each value of the phase uniquely determines the values of μ and ν via the formulas

$$\mu = |c_m|^2 m + |c_n|^2 n, \quad \text{(C3)}$$

$$\nu = (|c_m|^4 + |c_n|^4)^{-1}. \quad \text{(C4)}$$

It turns out that quantities μ and ν are correlated for each eigenfunction corresponding to localized resonance (48). This results in formation of "bridges" in the μ-ν plane.

[1] H. Morita and K. Kaneko, Phys. Rev. Lett. **96**, 050602 (2006).
[2] R. Bachelard, C. Chandre, D. Fanelli, X. Leoncini, and S. Ruffo, Phys. Rev. Lett. **101**, 260603 (2008).
[3] S. S. Abdullaev, Phys. Rev. E **84**, 026204 (2011).
[4] K. V. Koshel' and S. V. Prants, Phys. Usp. **49**, 1151 (2006).
[5] S. Prants, M. Budyansky, V. Ponomarev, and M. Uleysky, Ocean Model. **38**, 114 (2011).
[6] C. Conti, D. Rossinelli, and P. Koumoutsakos, J. Comput. Phys. **231**, 2229 (2012).
[7] H. Kantz and P. Grassberger, Physica D **17**, 75 (1985).
[8] G. Froyland, K. Padberg, M. H. England, and A. M. Treguier, Phys. Rev. Lett. **98**, 224503 (2007).
[9] G. Froyland and K. Padberg, Physica D **238**, 1507 (2009).
[10] D. Makarov and M. Uleysky, J. Phys. A: Math. Gen. **39**, 489 (2006).
[11] D. V. Makarov, M. Y. Uleysky, M. V. Budyansky, and S. V. Prants, Phys. Rev. E **73**, 066210 (2006).
[12] C. Gan, Q. Wang, and M. Perc, J. Physics A: Math. Theor. **43**, 125102 (2010).
[13] C. Gan and H. Lei, J. Sound Vibr. **330**, 2174 (2011).
[14] A. R. Kolovsky, Phys. Rev. E **56**, 2261 (1997).
[15] A. L. Virovlyansky, D. V. Makarov, and S. V. Prants, Phys. Usp. **55**, 18 (2012).
[16] D. Makarov, S. Prants, A. Virovlyansky, and G. Zaslavsky, *Ray and Wave Chaos in Ocean Acoustics: Chaos in Waveguides*, Series on Complexity, Nonlinearity and Chaos, Vol. 1 (World Scientific, Singapore, 2009).
[17] F. J. Beron-Vera, M. G. Brown, J. A. Colosi, S. Tomsovic, A. L. Virovlyansky, M. A. Wolfson, and G. M. Zaslavsky, J. Acoust. Soc. Am. **114**, 1226 (2003).
[18] K. B. Smith, M. G. Brown, and F. D. Tappert, J. Acoust. Soc. Am. **91**, 1939 (1992).
[19] I. P. Smirnov, A. L. Virovlyansky, and G. M. Zaslavsky, Phys. Rev. E **64**, 036221 (2001).
[20] M. G. Brown, J. A. Colosi, S. Tomsovic, A. L. Virovlyansky, M. A. Wolfson, and G. M. Zaslavsky, J. Acoust. Soc. Am. **113**, 2533 (2003).
[21] D. V. Makarov, M. Y. Uleysky, and S. V. Prants, Chaos **14**, 79 (2004).
[22] F. J. Beron-Vera and M. G. Brown, J. Acoust. Soc. Am. **115**, 1068 (2004).
[23] A. L. Virovlyansky and G. M. Zaslavsky, Phys. Rev. E **59**, 1656 (1999).
[24] I. P. Smirnov, A. L. Virovlyansky, and G. M. Zaslavsky, Chaos **14**, 317 (2004).
[25] I. P. Smirnov, A. L. Virovlyansky, M. Edelman, and G. M. Zaslavsky, Phys. Rev. E **72**, 026206 (2005).
[26] G. Tanner and N. Sondergaard, J. Physics A: Math. Theor. **40**, R443 (2007).
[27] L. E. Kon'kov, D. V. Makarov, E. V. Sosedko, and M. Y. Uleysky, Phys. Rev. E **76**, 056212 (2007).
[28] O. A. Godin, J. Acoust. Soc. Am. **122**, 3353 (2007).
[29] D. V. Makarov, L. E. Kon'kov, and M. Y. Uleysky, Acoust. Phys. **54**, 382 (2008).
[30] O. A. Godin, Acta Acustica **95**, 963 (2009).
[31] K. C. Hegewisch, N. R. Cerruti, and S. Tomsovic, J. Acoust. Soc. Am. **117**, 1582 (2005).
[32] W. Munk and C. Wunsch, Deep Sea Res. Part A. **26**, 123 (1979).
[33] F. D. Tappert and X. Tang, J. Acoust. Soc. Am. **99**, 185 (1996).

[34] V. Bezotvetnykh, A. Burenin, Y. Morgunov, and Y. Polovinka, Acoust. Phys. **55**, 376 (2009).
[35] R. C. Spindel, J. Na, P. H. Dahl, S. Oh, C. Eggen, Y. G. Kim, V. A. Akulichev, and Y. N. Morgunov, IEEE J. Ocean. Engin. **28**, 297 (2003).
[36] J. L. Spiesberger and F. D. Tappert, J. Acoust. Soc. Am. **99**, 173 (1996).
[37] P. F. Worcester, B. D. Cornuelle, J. A. Hildebrand, J. William, S. Hodgkiss, T. F. Duda, J. Boyd, B. M. Howe, J. A. Mercer, and R. C. Spindel, J. Acoust. Soc. Am. **95**, 3118 (1994).
[38] P. F. Worcester, B. D. Cornuelle, M. A. Dzieciuch, W. H. Munk, B. M. Howe, J. A. Mercer, R. C. Spindel, J. A. Colosi, K. Metzger, T. G. Birdsall, and A. B. Baggeroer, J. Acoust. Soc. Am. **105**, 3185 (1999).
[39] K. E. Wage, M. A. Dzieciuch, P. F. Worcester, B. M. Howe, and J. A. Mercer, J. Acoust. Soc. Am. **117**, 1565 (2005).
[40] N. S. Grigorieva, G. M. Fridman, J. A. Mercer, R. K. Andrew, M. A. Wolfson, B. M. Howe, and J. A. Colosi, J. Acoust. Soc. Am. **125**, 1919 (2009).
[41] I. A. Udovydchenkov, M. G. Brown, T. F. Duda, J. A. Mercer, R. K. Andrew, P. F. Worcester, M. A. Dzieciuch, B. M. Howe, and J. A. Colosi, J. Acoust. Soc. Am. **131**, 4409 (2012).
[42] K. C. Hegewisch and S. Tomsovic, Europhys. Lett. **97**, 34002 (2012).
[43] R. C. Shockley, J. Northrop, P. G. Hansen, and C. Hartdegen, J. Acoust. Soc. Am. **71**, 51 (1982).
[44] W. H. Munk, W. C. O'Reilly, and J. L. Reid, J. Phys. Oceanogr. **18**, 1876 (1988).
[45] *Oceanography and Marine Environment of the Far Eastern Region of Russia (proj. leader Rostov I. D.)* [http://www.pacificinfo.ru/en].
[46] L. M. Brekhovskikh, V. V. Goncharov, S. A. Dremuchev, V. M. Kurtepov, V. G. Selivanov, and Y. A. Chepurin, Sov. Phys. Acoust. **36**, 461 (1990).
[47] I. Smirnov, J. Caruthers, and A. Khil'ko, Radiophys. Quant. Electron. **42**, 864 (1999).
[48] A. K. Morozov and J. A. Colosi, J. Acoust. Soc. Am. **117**, 1611 (2005).
[49] Y. Petukhov, Acoust. Phys. **55**, 785 (2009).
[50] L. B. Dozier and F. D. Tappert, J. Acoust. Soc. Am. **64**, 533 (1978).
[51] H. J. Stöckmann, *Quantum Chaos: An Introduction* (Cambridge University Press, Cambridge, 2007), p. 384.
[52] G. M. Zaslavsky, *The Physics of Chaos in Hamiltonian Systems* (Imperial College Press, London, 2007), p. 328.
[53] I. I. Rypina, M. G. Brown, F. J. Beron-Vera, H. Koçak, M. J. Olascoaga, and I. A. Udovydchenkov, Phys. Rev. Lett. **98**, 104102 (2007).
[54] S. Soskin, R. Mannella, and P. McClintock, Phys. Rep. **373**, 247 (2003).
[55] A. I. Malyshev, Nelin. Dinam. **5**, 425 (2009) (in Russian).
[56] D. del Castillo-Negrete, J. M. Greene, and P. J. Morrison, Physica D **91**, 1 (1996).
[57] M. V. Budyansky, M. Y. Uleysky, and S. V. Prants, Phys. Rev. E **79**, 056215 (2009).
[58] M. Y. Uleysky, M. V. Budyansky, and S. V. Prants, Phys. Rev. E **81**, 017202 (2010).
[59] M. Uleysky, M. Budyansky, and S. Prants, J. Exp.: Theor. Phys. **111**, 1039 (2010).
[60] J. Simmen, S. M. Flatte, and G.-Y. Wang, J. Acoust. Soc. Am. **102**, 239 (1997).
[61] A. Sugita and H. Aiba, Phys. Rev. E **65**, 036205 (2002).
[62] D. N. Maksimov and A. F. Sadreev, Phys. Rev. E **77**, 056204 (2008).
[63] I. Varga and J. Pipek, Phys. Rev. E **68**, 026202 (2003).
[64] G. P. Berman and A. R. Kolovskĭ, Sov. Phys. Usp. **35**, 303 (1992).
[65] S. Fishman, D. R. Grempel, and R. E. Prange, Phys. Rev. Lett. **49**, 509 (1982).
[66] L. D. Landau and E. M. Lifshitz, *Course of Theoretical Physics*: *Quantum mechanics, Nonrelativistic theory*, Vol. 3 (Pergamon Press, Oxford, 1977).
[67] M. V. Berry and M. Robnik, J. Phys. A: Math. Gen. **17**, 2413 (1984).
[68] A. Bäcker, R. Ketzmerick, and A. G. Monastra, Phys. Rev. Lett. **94**, 054102 (2005).
[69] M. V. Berry, J. P. Keating, and S. D. Prado, J. Phys. A **31**, L245 (1998).
[70] A. Relaño, J. M. G. Gómez, R. A. Molina, J. Retamosa, and E. Faleiro, Phys. Rev. Lett. **89**, 244102 (2002).
[71] A. Relaño, Phys. Rev. Lett. **100**, 224101 (2008).
[72] K. Kudo and T. S. Monteiro, Phys. Rev. E **77**, 055203 (2008).
[73] J. A. Colosi and M. G. Brown, J. Acoust. Soc. Am. **103**, 2232 (1998).
[74] L. R. LeBlanc and F. H. Middleton, J. Acoust. Soc. Am. **67**, 2055 (1980).
[75] K. Mallick and P. Marcq, Phys. Rev. E **66**, 041113 (2002).